INTERFACE

rsif.royalsocietypublishing.org

Research

Cite this article: Lai X, Brown A, Xue C. 2018 A stochastic model that explains axonal organelle pileups induced by a reduction of molecular motors. *J. R. Soc. Interface* **15**: 20180430.
http://dx.doi.org/10.1098/rsif.2018.0430

Received: 11 June 2018
Accepted: 22 October 2018

Subject Category:
Life Sciences–Mathematics interface

Subject Areas:
computational biology

Keywords:
intracellular traffic jams, axonal transport, lattice-based model

Author for correspondence:
Chuan Xue
e-mail: cxue@math.osu.edu

A stochastic model that explains axonal organelle pileups induced by a reduction of molecular motors

Xiulan Lai[1], Anthony Brown[2] and Chuan Xue[3]

[1]Institute for Mathematical Sciences, Renmin University of China, Beijing, People's Republic of China
[2]Department of Neuroscience, and [3]Department of Mathematics, Ohio State University, Columbus, OH, USA

CX, 0000-0002-5482-8693

Nerve cells are critically dependent on the transport of intracellular cargoes, which are moved by motor proteins along microtubule tracks. Impairments in this movement are thought to explain the focal accumulations of axonal cargoes and axonal swellings observed in many neurodegenerative diseases. In some cases, these diseases are caused by mutations that impair motor protein function, and genetic depletion of functional molecular motors has been shown to lead to cargo accumulations in axons. The evolution of these accumulations has been compared to the formation of traffic jams on a highway, but this idea remains largely untested. In this paper, we investigated the underlying mechanism of local axonal cargo accumulation induced by a global reduction of functional molecular motors in axons. We hypothesized that (i) a reduction in motor number leads to a reduction in the number of active motors on each cargo which in turn leads to less persistent movement, more frequent stops and thus shorter runs; (ii) as cargoes stop more frequently, they impede the passage of other cargoes, leading to local 'traffic jams'; and (iii) collisions between moving and stopping cargoes can push stopping cargoes further away from their microtubule tracks, preventing them from reattaching and leading to the evolution of local cargo accumulations. We used a lattice-based stochastic model to test whether this mechanism can lead to the cargo accumulation patterns observed in experiments. Simulation results of the model support the hypothesis and identify key questions that must be tested experimentally.

1. Introduction

Axons are long cytoplasmic processes that extend from the cell bodies of neurons, enabling these cells to form synaptic connections with other cells throughout the body. The growth, maintenance and physiological function of axons are critically dependent on the intracellular transport of membranous organelles and macromolecular complexes [1,2]. The cargoes move anterogradely or retrogradely along microtubule tracks, propelled by kinesin and dynein motor proteins, respectively [3–5]. Axonal microtubules are polarized protein polymers that align in the axial direction of the axon, with their plus ends pointing away from the cell body. These microtubules can be hundreds of micrometres long, and each axon contains a continuous overlapping array of these polymers that extends along its entire length, ensuring the continuity of axonal transport.

Impairments of axonal transport are observed in many neurodegenerative diseases such as Charcot–Marie–Tooth disease, hereditary spastic paraplegia, spinal muscular atrophy, Parkinson's disease, Alzheimer's disease and motor neuron disease [6–12]. These diseases are often characterized by local axonal swellings containing accumulations of axonally transported cargoes both in human patients [13–16] and in animal models [17–20]. In many familial cases, these diseases are caused by mutations in proteins involved in intracellular transport, including mutations that impair the activity of the motor proteins [21–27]. However, little

THE ROYAL SOCIETY PUBLISHING

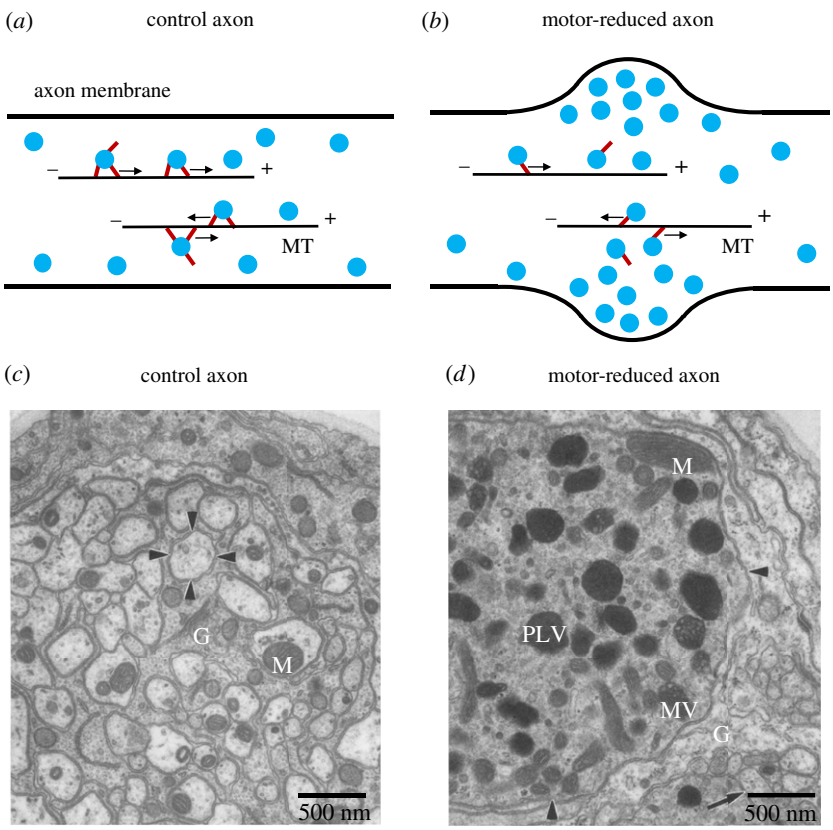

Figure 1. Axonal swelling and organelle pileups induced by a genetic depletion of functional kinesin motors. (*a*) Schematic drawing that illustrates the intracellular transport of cargoes in a segment of a control axon. The cyan discs represent axonal organelles and the red line segments represent motor proteins on the surface of the organelles. (*b*) Schematic drawing that illustrates the focal accumulation of organelles in a swollen axon due to a reduction in the number of functional motors. (*c*,*d*) Electron micrographs of control and kinesin mutant axons in *Drosophila* larval segmental nerves adapted from fig. 2C,D in [28]. The kinesin mutation was a hypomorphic missense mutation in the kinesin-1 heavy chain that resulted in a depletion of functional kinesin-1 motors. The authors compared the nerve ultrastructure in control and kinesin mutant larvae. Full experimental details can be found in the original article. (*c*) An electron micrograph of a cross section of a control segmental nerve. Arrowheads point to the plasma membrane of one axon. Cytoplasmic processes of the surrounding glial cells (G) extend throughout the nerve, ensheathing many of the axons. The axon diameters in the control nerve vary from ~100 to 700 nm. Mitochondria (M), vesicles (~30–60 nm) and a few small multi-vesicular bodies are seen in the axons. (*d*) A swollen axon in a kinesin mutant segmental nerve. The arrowheads point to the plasma membrane of the swollen axon, which is many times larger than the control axons. The swelling is engorged with mitochondria, vesicles, multi-vesicular organelles (MV) and large dark prelysosomal vacuoles (PLV). The arrow in the lower right points to an adjacent axon that is not swollen in this plane of section. The scale bars are 500 nm. (Online version in colour.)

is understood about the underlying mechanisms that lead to organelle accumulations in these situations.

Axonal swellings containing accumulations of axonally transported cargoes have also been observed in fly nerves when functional kinesin and dynein motors were reduced gradually during larval development [28,29] (see figure 1). These authors concluded that gradual depletion of kinesin or dynein motors caused axonally transported cargoes to stall, generating traffic jams and organelle pileups. Organelle traffic jams have also been observed in axons of cultured fly nerve cells using live cell imaging [30]. These authors found that depletion of kinesin or dynein motors resulted in two types of focal organelle accumulations: static pileups, which persisted throughout the observation time period, and dynamic pileups, which dispersed (i.e. resolved) during the observation period. They hypothesized that these pileups formed when stalled cargoes impeded the movement of other cargoes. More recently, organelle traffic jams have also been described at actin-rich regions of axons in *Caenorhabditis elegans* [31]. These authors observed that stationary vesicles at actin-rich regions increased the propensity of other moving vesicles to stall at the same location, resulting in traffic jams arising from physical crowding.

Mathematical models for axonal transport of various cargoes have been developed previously. In these models, cargoes are described as non-interacting particles that move independently [32–43]. However, to explain organelle traffic jams in axons, the potential steric effects created by the large size of membranous cargoes must be considered. For example, axonally transported membranous organelles can range from 50 to 500 nm in diameter [44,45], yet the microtubule tracks along which they move measure just 25 nm in diameter. Moreover, a single microtubule can support both anterograde and retrograde movement simultaneously [46,47]. Thus, there is the potential for cargoes that move along microtubules to collide and interfere with each other's movement, particularly for large cargoes or at high cargo densities. Previous computational models developed in [48–52] investigated conditions that cause accumulations of unloaded motor proteins on microtubules, but did not explain how a reduction of motors might lead to organelle accumulations such as described in [28,30]. In addition, cargo accumulation is fundamentally different from motor crowding because one cargo can be transported by multiple motors and motors can, in principle, bind and dissociate from cargoes reversibly during cargo transport.

Since single cargoes are believed to bind multiple motors, a direct consequence of lower motor number is decreased run lengths and more frequent stalls [53,54]. This is because the probability of a cargo dissociating from its microtubule

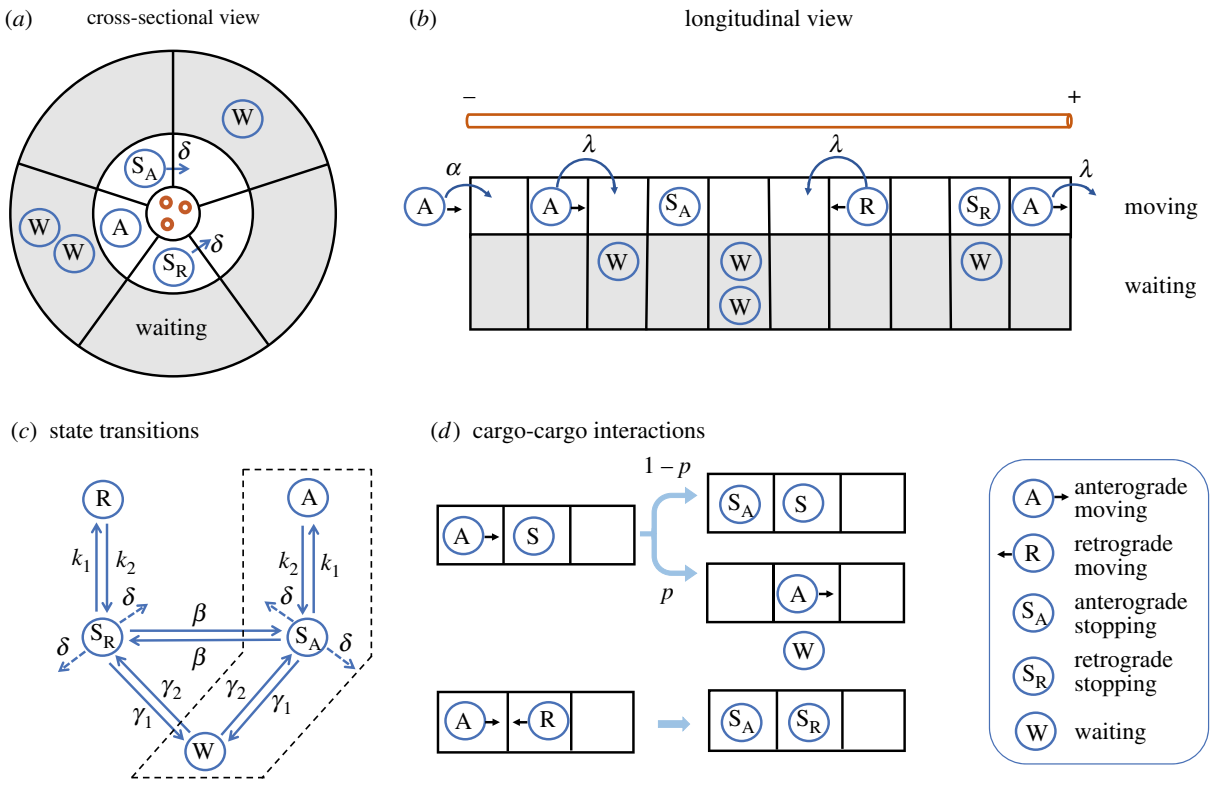

Figure 2. Model set-up. (*a*) Cross-sectional view of a cluster of microtubules. The space around the microtubules was considered to be subdivided into five sectors. Each sector was considered to be one lane for organelle movement and was subdivided into an inner moving zone (white) and an outer waiting zone (grey). The blue circles represent organelle cargoes (not drawn to scale), and the arrows represent transitions between the tracks. (*b*) Longitudinal view of one sector, showing the moving and waiting zones (white and grey, respectively), which were subdivided longitudinally into 'boxes' that represented steps along the microtubule track. Boxes in the moving zone could be occupied by only one cargo at a time, but boxes in the waiting zone could contain multiple cargoes. Movement of cargoes was modelled as transitions between consecutive boxes in the moving state, either towards the '+' end of the microtubules (anterograde direction) or towards the '−' end (retrograde direction). (*c*) Diagram representing the stochastic cargo state transitions. The bounded region shows the scheme for the special case of anterograde traffic only. (*d*) Major crowding rules for cargo–cargo interactions. Here S stands for either S_A or S_R. All parameters are defined in table 1. (Online version in colour.)

track increases if fewer motors are mediating that interaction. We speculate that these stalled cargoes can in turn impede the passage of other moving cargoes on those same microtubule tracks, increasing their probability to stall as well and that incoming cargoes can push stalled cargoes away from their microtubule tracks, preventing them temporarily from reattaching to microtubules. We hypothesize that this kind of positive feedback can cause the local cargo accumulations observed in [28,30], and that no extra mechanisms are needed to explain these 'axonal traffic jams'.

In the present study, we tested this hypothesis using a stochastic, on-lattice model for axonal transport that integrates cargo–cargo mechanical interactions. We treated the axon as a highway comprised of multiple moving lanes and waiting zones. We divided each lane/zone into longitudinal boxes and modelled the cargo movement as a position jump process. We first considered the simplified situation in which cargoes moved in a single lane and in only one direction. We then expanded the model to allow for multiple lanes with the possibility of lane-switching. Finally, we investigated the influence of bidirectional transport of cargoes on collisions and accumulations. In §2, we describe the model and the underlying assumptions in detail. In §3, we present simulations of the model with increasing complexities using parameters estimated from experimental data. The simulation results support our hypothesis described above. Finally, we conclude and discuss the implications of our findings in §4.

2. The mathematical model

2.1. Description of the model

We described axonal cargoes as individual particles that moved stochastically along the axon and interacted with each other through volume exclusion. We adopted a lattice-based approach for cargo transport (figure 2).

There are multiple microtubules in each cross section of an axon, which are often clustered in groups [55], and each microtubule can support the movement of multiple cargoes. Moreover, organelles usually have multiple molecular motors attached to their surfaces, and these motors can simultaneously interact with different microtubules or with different protofilaments on the same microtubule.

Based on these considerations, we considered each axon to be comprised of longitudinal channels, each centred on a microtubule or a cluster of several microtubules. Small axons might have a single channel whereas large axons might comprise multiple channels. For the present study, we considered the case of a single channel. In cross section, the space around the microtubule or cluster of microtubules in each channel was divided into five radial sectors, each with an inner shell (moving zone) and an outer shell (waiting zone) as in figure 2*a*. We chose five based on the consideration of the geometry of the small microtubule clusters. The results were qualitatively the same if we varied the number of radial sectors. The moving zones can be considered to be

analogous to the 'lanes' of a highway and the waiting zones to 'parking spaces' on the side of a highway. We assumed that cargoes in a moving zone were in close proximity to the microtubule tracks and were thus available to be transported along them, and that cargoes in a waiting zone were farther from the microtubule tracks and were thus not capable of being transported until they diffused into a moving zone.

Longitudinally, we divided these sectors and zones into contiguous segments, which we will refer to as boxes, and described cargo movement as positional jumps (forwards or backwards) from one box to a neighbouring box (figure 2*b*). Cargoes could only enter and exit the axon through the boundary boxes, which represent the proximal and distal ends of a short axonal segment. We assumed that only a single cargo could fit in one moving zone box (white box), but multiple cargoes could fit in one waiting zone box (grey box).

To model cargo movement, we did not make any assumptions about the mechanism or kinetics of motor binding to cargoes or microtubules. Instead, we described each cargo by its position in the axon and its movement state, similar to [39]. In particular, we assumed that each cargo existed in one of five states: moving anterogradely, moving retrogradely, stopping anterogradely, stopping retrogradely and waiting (figure 2*c*). The first four states were associated with a moving zone, and the last state was associated with a waiting zone. Stopping cargoes started to move with rate k_1 and moving cargoes stopped with rate k_2. Cargoes could switch their direction of movement with rate β, but only when they were in a stopping state. They could also switch to a neighbouring lane with rate δ, but again only if they were stopping. Finally, stopping cargoes could move to the waiting zone with rate γ_1 and waiting cargoes could switch to the moving zone with rate γ_2. In our simulations, we also considered a simplified case in which all cargoes moved unidirectionally (e.g. anterogradely). The diagram for this special case is illustrated by the bounded region in figure 2*c*.

For the case of unidirectional transport, all cargoes entered the proximal end of the axon with influx rate α and then moved anterogradely along the microtubules (towards their plus ends) by transitioning from one box to the next as shown in figure 2*b*. We started each simulation with an empty axon. For the case of unidirectional transport, we allowed the cargoes to enter at the proximal end (left) and leave at the distal end (right). An anterogradely moving cargo in box i hopped to the next box $(i+1)$ with rate λ. However, if box $(i+1)$ was occupied by a stopping cargo, then the moving cargo either stopped moving or pushed the stopping cargo away from the microtubule track into the corresponding waiting zone (figure 2*d*). For the case of bidirectional transport, cargo were allowed to enter and leave the axon domain at either end. Cargo entering at the proximal (left) end were initially anterograde, and cargo entering the distal (right) end were initially retrograde. To preserve the overall cargo density in the case of bidirectional transport, the influx rate at either end was set to be $\alpha/2$. Retrogradely moving cargoes were treated in the same way as anterograde cargoes, except with movement in the opposite direction. If two cargoes moving in the opposite direction bumped into each other, then we switched the states of both cargoes to the corresponding anterograde and retrograde stopping states. In addition, we did not allow movement of waiting or stopping cargoes if their destination was occupied by other cargoes. Specifically, we rejected the movement from a waiting zone to a moving zone or from one lane to another if the destination was occupied by a cargo.

Let A_i^j, R_i^j, SA_i^j, SR_i^j, W_i^j denote the number of cargoes in each of the five states, respectively in the ith segment and the jth sector. The state of the axon is then represented by $\{A_i^j, R_i^j, SA_i^j, SR_i^j, W_i^j : 1 \le i \le N, 1 \le j \le 5\}$. Cargo state transitions and cargo movement are events that potentially cause system state changes. For example, the transition of an anterogradely moving cargo to stopping in the (i, j)th box leads to the system state change

$$(A_i^j, SA_i^j) \to (A_i^j - 1, SA_i^j + 1),$$

with propensity $\rho = k_2 A_i^j$. To simulate the model, we asynchronously updated the dynamic state of the axon using a method similar to Gillespie's method [56,57]. For each step, we first determined the waiting time τ for the next potential event and for which event. We then took into account the crowding rules to either accept or reject the event and update the system state. The typical time step of the simulations was of the order of milliseconds which was determined by the algorithm.

2.2. Parameter estimation

We estimated the parameters of the model based on experimental measurements. The parameter values are summarized in table 1, and the estimation methods are described below.

The speed of organelle movement in axons ranges from 0.5 to 5 $\mu m\, s^{-1}$ [58,59]. For the present study, we assumed a speed of $s_0 = 1\ \mu m\, s^{-1}$ and that each box was about $d = 1\ \mu m$ long. Thus the cargo moving rate λ could be estimated as $d/s_0 = 1\ s^{-1}$. The cargo influx rate α was inferred from simulations to make sure that the overall cargo density was comparable to experimental data for control axons [44]. We assumed that when a cargo transitioned from moving to stopping it remained in close proximity to the microtubule track and that its transition back to the moving state was governed by the binding rate of motor to microtubule and set to be $k_1 = 5\ s^{-1}$, which is consistent with the modelling studies of [60].

We assumed that cargoes in the waiting state were farther from their microtubule tracks and that they had to make a diffusional encounter with the microtubule track in order to resume movement. Thus, we assumed that the transition between stopping and waiting states was governed by Brownian motion of the organelles. The diffusion coefficient of an organelle was estimated to be $D = 1.02 \times 10^{-4}\ \mu m^2\, s^{-1}$ in [61]. We assumed that a cargo in a waiting zone needed to move a distance $l = \frac{1}{3}$ m to the moving zone to become a stopping cargo and vice versa. Then the rates γ_1, γ_2 could be estimated as $D/l^2 \approx 10^{-3}\ s^{-1}$.

The run length of a cargo *in vitro* is dependent on the processivity of the motors and the number that are bound to the cargo [54,60]. The more processive a motor, the more steps it takes per diffusional encounter with its microtubule track. The more motors that are bound to a cargo, the lower the probability that all will detach simultaneously. Moreover, if one or more motors remain attached, those that detach remain tethered close to the microtubule and thus have a higher reattachment rate. Thus, the cargo run length is sensitive to the number of bound motors. In our model, this was realized in k_2, which is the rate of transition between moving and stopping states. In control axons, a moving organelle is believed to have multiple active motors on its surface and to move persistently inside the axon with a small k_2. However, if the overall concentration

Table 1. Model parameters.

parameter	description	value
λ	cargo moving rate per lane	$1\,s^{-1}$
α	cargo influx rate per lane	$0.02\,s^{-1}$
k_1	transition rate from stopping to moving	$5\,s^{-1}$
k_2	transition rate from moving to stopping	$0.05\,s^{-1}$ for control, $5\,s^{-1}$ for motor-reduced
γ_1	transition rate from stopping to waiting	$10^{-3}\,s^{-1}$
γ_2	transition rate from waiting to stopping	$10^{-3}\,s^{-1}$
β	reversal rate	$0-1\,s^{-1}$
p	cargo persistency (between 0 and 1)	1 for control, 0.2 for motor-reduced
δ	lane-switching rate	$1\,s^{-1}$

of the molecular motors is reduced, as occurred in [28,30], then we assumed that there would be fewer motors on the cargo and it would move less persistently (i.e. stop more frequently) with a large k_2. In our simulations, we set k_2 to be $0.05\,s^{-1}$ for control axons and $5\,s^{-1}$ for motor-reduced axons. These values are comparable with experimental measurements of the average run length of cargoes in axons and the dissociation rate of a single molecular motor from a microtubule [62].

In axons, moving organelles will encounter obstacles such as other organelles that will increase the drag on the bound motors and thus increase the probability of motor detachment from the microtubule track, which will cause the cargo to stop. If a moving cargo has enough active motors pulling it forward, the force acting on the moving cargo may be large enough to push a stopping cargo away from the microtubule track, allowing the moving cargo to continue uninterrupted. In our model, this was realized as the cargo persistency parameter p. For a large number of motors, we set p to be 1. A reduction in motor number was modelled as a reduction in p. In our simulations, we set p to be 1 for control axons and 0.2 for motor-reduced axons.

The parameter values used in all the simulations were the same as in table 1 unless otherwise noted.

3. Results

3.1. A simplified case: unidirectional transport in a single lane

In intracellular traffic, collisions can occur between moving and stopping cargoes as well as between cargoes moving in opposite directions. Cargoes can navigate collisions by pushing other cargoes aside or by switching 'lanes' (e.g. between adjacent microtubules, or between adjacent protofilaments within the same microtubule). Thus, the directionality of traffic and the number of parallel 'lanes' available can influence both the cargo interactions and accumulation. We first considered the simplest case of a single lane of unidirectional traffic and then subsequently incorporated these complexities.

We simulated cargo movement in a domain that represents a short segment of a long axon. We started with an empty axon and allowed cargoes to enter the left-most box (equivalent to the proximal end of the axon) randomly with rate α. We recorded the spatial cargo distribution in the domain over time and generated plots with time in the vertical dimension and distance in the horizontal dimension. These plots are similar to kymographs, which have been used extensively in experimental studies [63].

Figure 3*a* shows an example in which the spatial–temporal cargo distribution was sampled every 36 s in a 30 min time window for one realization of the model with $k_2 = 5\,s^{-1}$. Here black represents one or more cargoes at that location and time, and white means no cargo present. The black dots mainly represent moving and stopping cargoes in the moving zone and the black vertical lines represent cargoes in the waiting zone.

While figure 3*a* reveals the overall density and dynamics of the traffic over time, the continuous movement of individual cargoes can only be seen if we sample more frequently in time. Figure 3*b* plots the cargo distribution sampled every 0.36 s, that is, 100 times more frequently, in the time window between 4.8 and 7.8 min and between 18 and 21 min. These plots show several notable events, specifically a cargo in the moving zone that transitioned to the waiting zone around $t = 5.6$ min (blue circle A), the same cargo which transitioned back to the moving zone and resumed movement around $t = 7.2$ min (blue circle B), and a moving cargo that pushed a stopping cargo aside around $t = 19.4$ min (blue circle C). Such events explain the start and end of each vertical line in figure 3*a*.

3.1.1. A reduction of motor number leads to dynamic cargo pileups

To investigate how motor reduction affects unidirectional transport on a single lane, we simulated the model over a time period of 24 h and recorded cargo distribution every 6 min for both control and motor-reduced axons. We used $k_2 = 0.05\,s^{-1}$ and $p = 1$ for the control case, as specified in table 1. The spatial–temporal distribution of all the cargoes, cargoes in the waiting zone, and cargoes in the moving zone in a single realization is plotted in figure 4*a*. The number of cargoes at a given point in space and time is depicted by the intensity according to the scale shown to the right of each plot. Pileups, which we defined as accumulations of ≥ 3 cargoes at the same location (depicted here as dark vertical lines), were rare.

In motor-reduced axons, cargoes on average have fewer motors on their surface. This could arise in disease, for example, due to mutations that alter the expression or function of a motor protein (see Introduction). We model the effect of fewer motors using a larger stopping transition rate

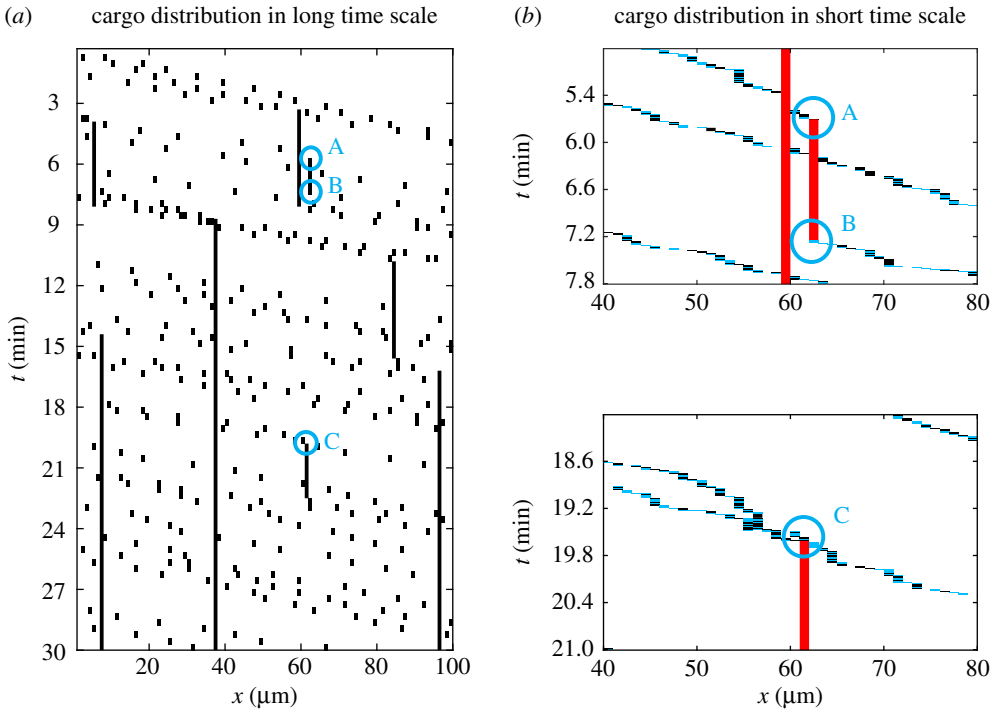

Figure 3. Illustration of cargo distribution plotted on coarse and fine time scales. (*a*) Cargo distribution plotted every 36 s. The long vertical lines indicate the waiting cargoes. (*b*) Cargo distributions plotted every 0.36 s. Blue, black, and red are used to label moving, stopping and waiting cargoes, respectively. The circles in (*b*) correspond to the circles in (*a*). A, a cargo in the moving zone transitioned to the waiting zone. B, a cargo in the waiting zone transitioned to the moving zone and resumed anterograde movement. C, a moving cargo pushed a stopping cargo to the waiting zone. The events depicted in A, B and C explain the start and end of each vertical line in (*a*). Parameters used: $k_2 = 5\,s^{-1}$, $p = 0.2$. Other parameter values were the same as in table 1. (Online version in colour.)

k_2 and a smaller persistant rate p when they encounter an obstacle, leading to shorter run lengths and more frequent and sustained stops. We used $k_2 = 5\,s^{-1}$, $p = 0.2$ for this case, as specified in table 1. Figure 4*b* plots the cargo distributions in a single realization. Comparison with the control axon in figure 4*a* shows that there was an overall increase in the traffic density and that this was due in large part to more cargoes in the waiting state. Pileups (evident as dark vertical lines) also occurred more frequently but remained dynamic: they could persist for several hours but always resolved.

Figure 4*c*,*d* plots the statistics of the cargo number in the whole domain for each case. The lines represent the total cargo number averaged over 100 realizations and the error bars represent the standard deviations. For the control axon, there were only a few cargoes in the 100 μm-long lane, and most of them were in the moving state. For the motor-reduced axon, the cargo numbers in the waiting and stopping states were significantly greater than in the control. Since we started each simulation with an empty axon, the initial number of cargoes in the domain was zero. As cargoes fluxed in to the left end of the domain, there was a surge in the total cargo density during the first few hours, which then reached a dynamic equilibrium with an average of $\geq$10 cargoes in the entire domain, which corresponds to $\geq$0.1 cargoes/μm (i.e. 0.1 per box in figure 2*b*).

To investigate the factors that influence the formation and dispersal of organelle pileups, we analysed how their number and lifespan depended on the stopping transition rate k_2 and the cargo persistency p. For each parameter combination, we averaged the results of 100 realizations and plotted the distribution of pileups that persisted for 0.5–15 h. Again, we defined a pileup as an accumulation of $\geq$3 cargoes in the same location. In figure 5*a*,*b* we see that the distributions were exponential in form. Figure 5*a* shows that the number of pileups increased with increasing values of k_2. This is expected because k_2 dictates the stopping frequency, and thus high values of k_2 should result in more stalled cargoes and more cargo collisions. Figure 5*b* shows that the number of pileups also increased with increasing values of p when the stopping transition rate was large ($k_2 = 5\,s^{-1}$). This is because large values of p allow the moving cargoes to push the stalled cargoes aside to the waiting zone when they collide. However, the cargo persistency has little effect on the pileups at low stopping transition rates because low stopping transition rates result in few stalled cargoes and thus few collisions (data not shown).

We next investigated the dependency of the fraction of moving, stopping and waiting cargoes on the rates k_2 and p, again averaging over 100 realizations. Figure 5*c* shows that most of the cargoes were moving when the stopping transition rate k_2 was small. For example, more than 70% of cargoes were moving for $k_2 < 0.5$. Figure 5*d* shows that the fraction of cargoes in the stopping state was highest when the stopping transition rate k_2 was large and the cargo persistency p was small, but not when p was large. This is because moving cargoes will tend to stop when they encounter other moving or stopping cargoes when the cargo persistency is low, increasing the number of stopped cargoes in the moving zone. By contrast, when the cargo persistency is high moving cargoes will tend to push any obstructing cargoes aside into the waiting zone. The highest proportion of waiting cargoes is thus encountered when both the stopping transition rate k_2 and the cargo persistency p are high, as shown in figure 5*e*.

3.1.2. Cargo crowding leads to static cargo pileups

In the previous simulations, we assumed that the state transition rates and movement speed are constants in the whole

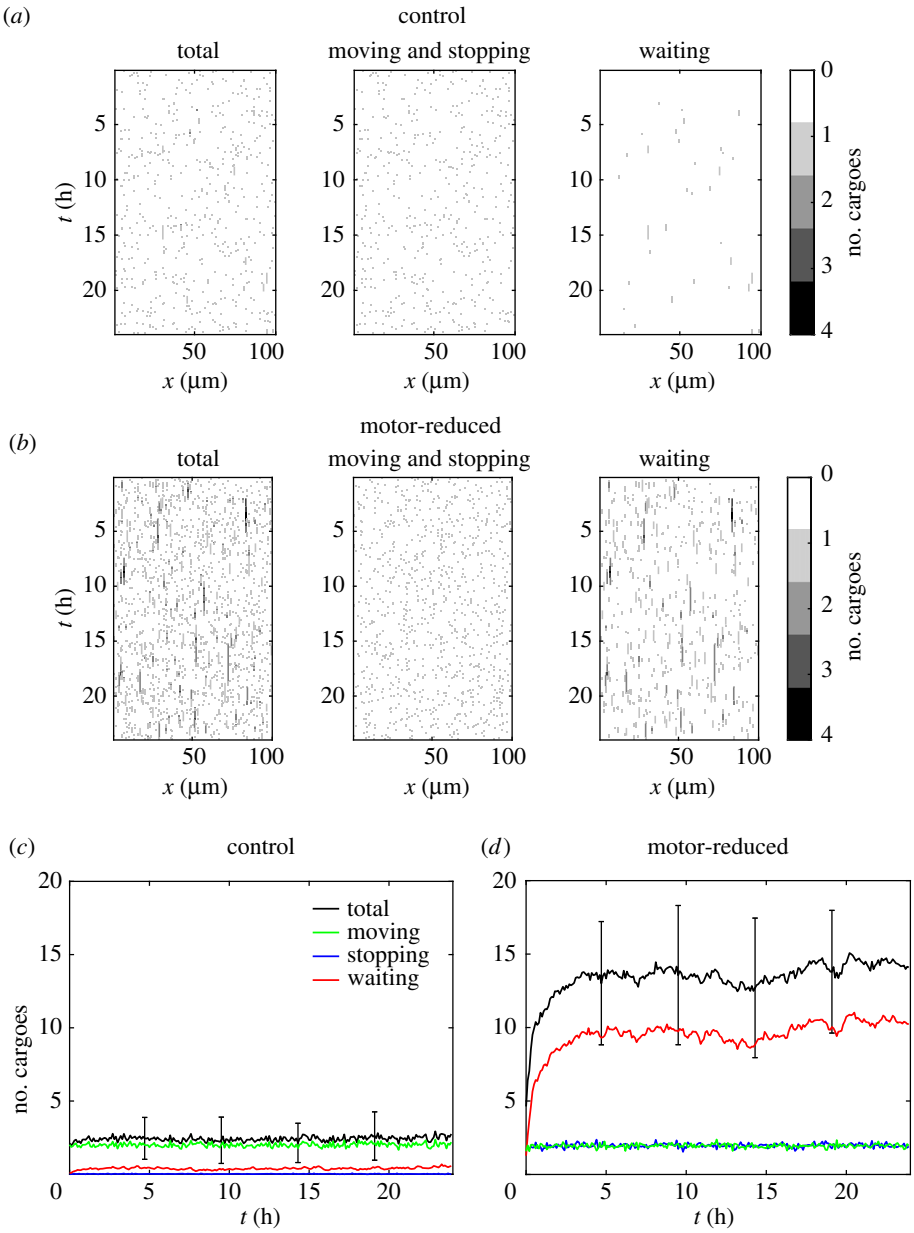

Figure 4. Spatial and temporal distribution of cargoes with unidirectional transport in a single lane. The simulation started with an empty axon and cargoes entered from the proximal (left) end. The time was measured from the start of the simulation. (*a*) Control axon, with $k_2 = 0.05\ s^{-1}$, $p = 1$. (*b*) Motor-reduced axon, with $k_2 = 5\ s^{-1}$, $p = 0.2$. Left: cargo number in all states. Middle: cargo number in the moving zone, including both moving and stopping cargoes. Right: cargo number in the waiting zone only. The number of cargoes at a given point in space and time (ranging from 0 to 4) is depicted by the intensity scale shown to the right of each plot. (*c*,*d*) Traffic density statistics in the whole domain for the control axon and the motor-reduced axon respectively. The data are the average of 100 realizations. The error bars indicate the standard deviation about the mean. Other parameter values were the same as in table 1.

domain. However, if cargoes accumulate locally, they will become more tightly packed at those locations, which could increase the force required to push them aside, and thus decrease the moving rate λ, or increase the probability of detachment, and thus increase the stopping transition rate (k_2). Thus, we investigated the feedback effect of local cargo density on the formation of organelle pileups.

We redefined the moving rate in box i to be

$$\lambda_i = \frac{\lambda}{1 + \eta[a_i W_i + (1 - a_i) W_{i+1}]},$$

where W_i represents the number of waiting cargoes in the ith box, a_i is the weight for W_i and η is a dimensionless constant with value $0 < \eta \leq 1$. We assumed that the waiting cargoes in the ith box and $(i+1)$th box exerted a negative feedback on the movement of the cargo in the ith box, and that the feedback effect of waiting cargoes in the ith box was slightly stronger ($a_i = 0.6$) compared to in the $(i+1)$th box ($1 - a_i = 0.4$).

For normal axons, simulation results with this nonlinear moving rate λ_i were similar to the results with constant λ shown in figure 4*a* (data not shown). For motor-reduced axons, figure 6*a* shows that persistent cargo pileups were observed with the nonlinear moving rate λ_i, where η was chosen to be 0.3. Overall, 65.9% of 1000 simulations exhibited one or more persistent pileups, which we defined as accumulations of ≥3 cargoes that lasted for ≥5 h. The spatial distribution of these pileups is shown in figure 6*c*. Note that pileups were observed throughout the axonal domain. The higher frequency of pileups in the proximal region (left side of the plot) is a boundary effect due to the entry of cargoes exclusively at the proximal (left) end of the axon.

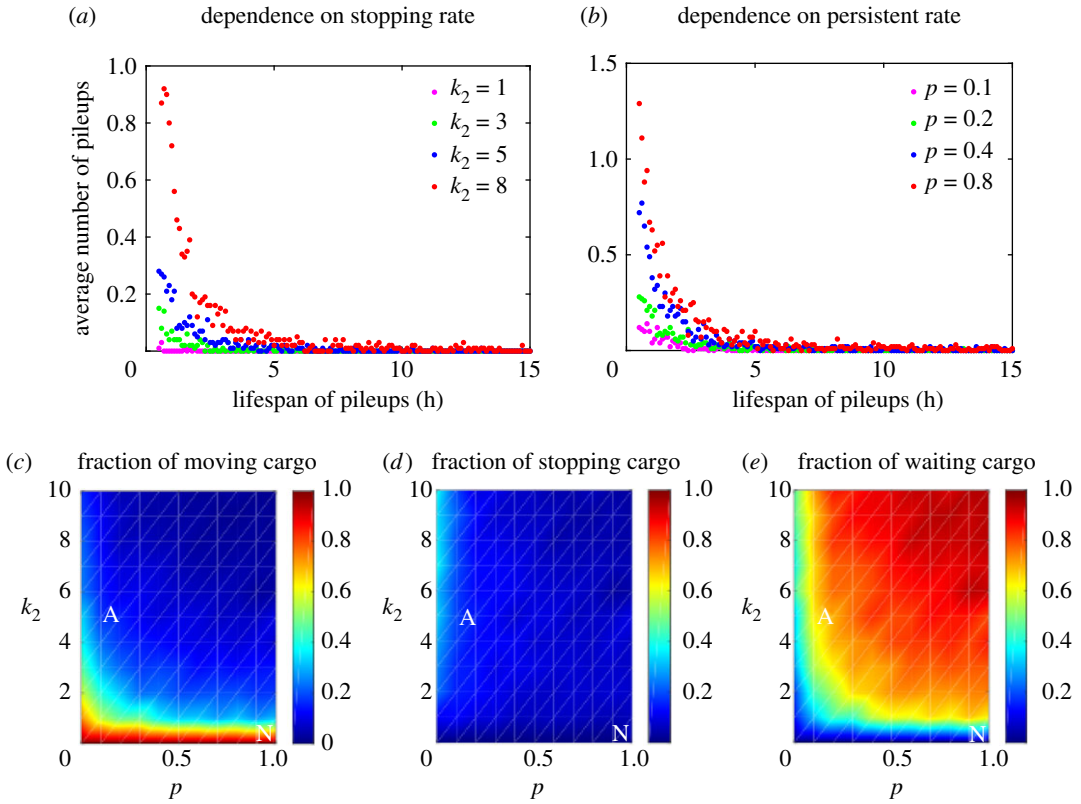

Figure 5. The statistics on the frequency of pileup formation, pileup lifespan, and the percentage of moving, stopping, and waiting cargoes in the motor-reduced case of unidirectional transport in a single lane. Pileups were defined as accumulations of ≥ 3 cargoes at the same location. Each plot represents the data averaged over 100 realizations. (*a*,*b*) The average number of pileups increases with increasing stopping transition rate k_2 (*a*) and with increasing cargo persistency p (*b*) for all pileup lifespans. (*c*) The percentage of moving cargoes was highest when the stopping transition rate k_2 was small, regardless of cargo persistency. (*d*) The percentage of stopping cargoes was highest when the stopping transition rate k_2 was large and the cargo persistency p was small. (*e*) The percentage of waiting cargoes was lowest when the stopping transition rate k_2 was small. The colour key represents the fraction of the total cargoes in the corresponding state. The point *N* denotes the control case and the point *A* represents the motor-reduced case. In (*a*), $p = 0.2$; in (*b*), $k_2 = 5\,\mathrm{s}^{-1}$. All other parameters were the same as in table 1.

Another way to introduce the crowding effect is to redefine the stopping transition rate in box i to be

$$k_2^i = k_2 \times [1 + \varepsilon(a_i W_i + (1 - a_i) W_{i+1})],$$

where ε is a dimensionless constant with value $0 < \varepsilon \leq 1$. For normal axons, simulation results with this nonlinear stopping transition rate k_2^i were similar to the results with constant k_2 shown in figure 4*b* (data not shown). For motor-reduced axons, figure 6*b* shows that persistent pileups were observed with the nonlinear stopping transition rate k_2^i, where ε was chosen to be 0.3. Overall, 52.5% of 1000 simulations exhibited one or more persistent pileups. The spatial distribution of these pileups is shown in figure 6*d*. Thus, simulation of cargo crowding using a nonlinear moving or stopping transition rate resulted in more persistent cargo accumulations.

3.2. Unidirectional transport in multiple lanes

We next considered the case of unidirectional transport with multiple lanes, allowing for the possibility of lane-switching. The number of lanes chosen was five (figure 2). The baseline parameters were chosen to be the same as for the single lane case above unless otherwise noted. The influx rate α was set to be $\alpha = 0.01 \times N_L$, where $N_L = 5$ is the lane number. In addition, we took the lane-switching rate to be $\delta = 1\,\mathrm{s}^{-1}$.

The values of p and k_2 were chosen to be the same as for the simulations of a single lane of traffic in normal and motor-reduced axons (see above). For normal axons, the simulation results for multiple lanes were similar to that observed for a single lane (compare figures 7*a* and 4*a*, and note that the intensity scales are different). For motor-reduced axons, the cargo dynamics in each lane demonstrated local accumulations, similar to the single lane model. However, these accumulations occurred at different locations in different lanes. When counted together, the total cargo density was more or less uniform in space (see figure 7*b*).

We next considered the nonlinear effect of cargo crowding in the multiple lane models. Here, the crowding effect was introduced using a weighted average of the cargoes in all lanes at that location along the axon, with cargoes in more proximate lanes creating more of an obstacle than those in more distant lanes. We redefined the moving rate in box i and lane j to be

$$\lambda_{ij} = \frac{\lambda}{1 + \eta \sum_{j=1}^{N_L} b_j [(a_i W_{i,j} + (1 - a_i) W_{i+1,j}]},$$

where $W_{i,j}$ represents the number of waiting cargoes in the ith box, jth lane, a_i and b_j are the weights and $0 < \eta \leq 1$. We took the weights to be $a_i = 0.6$, $b_j = 1$ for $W_{i,j}$, $b_j = 0.5$ for $W_{i,j-1}$ and $W_{i,j+1}$, and $b_j = 0.25$ for $W_{i,j-2}$ and $W_{i,j+2}$, and similarly for the waiting cargoes in the $(i + 1)$th box.

For normal axons, simulation results with this nonlinear moving rate $\lambda_i j$ were similar to the results with constant λ shown in figure 7*a* (data not shown). By contrast, in motor-reduced axons, we observed excessive local accumulations of cargoes that persisted for a long time, as shown in figure

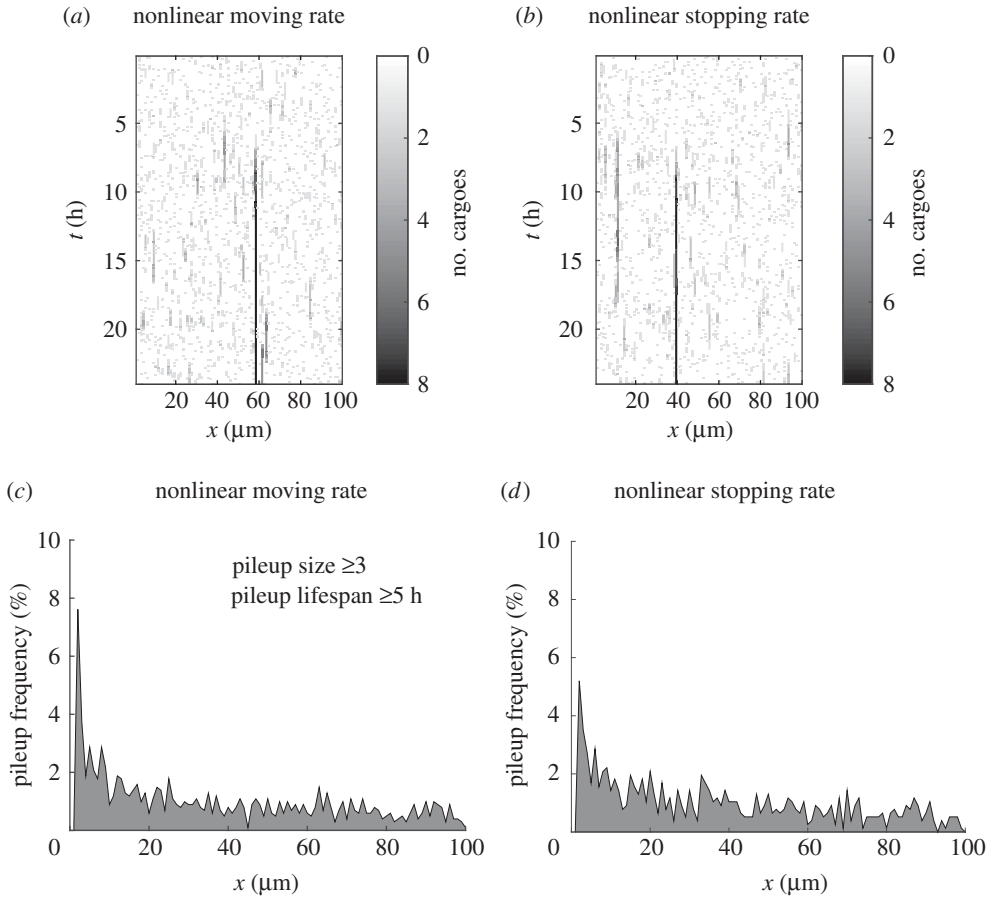

Figure 6. Spatial and temporal distribution of total cargoes in motor-reduced axons for unidirectional transport in a single lane with a nonlinear moving or stopping transition rate. More persistent accumulations of cargoes arose with either (*a*) a nonlinear moving rate λ_i or (*b*) a nonlinear stopping transition rate k_2^i. The parameters were chosen as in table 1 with $k_2 = 5\,s^{-1}$ and $p = 0.2$, and $\eta = 0.3$ and $\varepsilon = 0.3$ in the nonlinear terms of k_2^i and λ_i. (*c*,*d*) Spatial distribution of pileups (defined as accumulations of $\geq$3 cargoes with a lifespan of $\geq$5 h). Data obtained with 1000 realizations for nonlinear λ_i and k_2^i. The parameters were the same as in (*a*) and (*b*), respectively. The elevated number of cargo accumulations at the proximal (left) end of the domain is a boundary effect due to the entry of cargoes exclusively at the proximal (left) end of the axon.

7*c*, which is in agreement with the experiments by Hurd & Saxton [28]. Thus, the nonlinear crowding effect has the effect of synchronizing the dynamics in different lanes.

An alternative way to implement the cargo crowding effect with multiple lanes is to redefine the stopping transition rate in box i and lane j to be

$$k_2^{ij} = k_2\left[1 + \varepsilon \sum_{j=1}^{N_L} b_j(a_i W_{i,j} + (1 - a_i)W_{i+1,j})\right].$$

Simulation results using this approach were similar to the case with nonlinear λ (data not shown).

To quantify the extent of cargo accumulation in these simulations, we performed 1000 realizations and calculated the total number pileups that persisted for $\geq$5 h. Since the number of lanes of traffic was increased to 5, we redefined a pileup as the accumulation of $\geq$15 cargoes at a single location along the axon (five times greater than for our simulations of one lane of traffic). Overall, we observed one or more pileups with $\geq$15 cargoes lasting $\geq$5 h in 52.5% of the simulations. The spatial distribution of these pileups is shown in figure 7*d*. Note that pileups were observed throughout the axonal domain but were elevated in the proximal region (left side of plot) due to the boundary effect discussed above.

3.3. Bidirectional transport in multiple lanes

So far, we have considered only the case of unidirectional transport, yet organelles move bidirectionally in axons. To explore the effect of this two-way traffic, we investigated the effect of permitting cargoes to move retrogradely as well as anterogradely, still considering multiple lanes of traffic and allowing for switching between lanes. Cargoes were allowed to enter the axon from both the proximal and distal ends of the domain (left and right, respectively). Those entering at the proximal end were all initially moving anterograde state, and those entering at the distal end were all initially in the retrograde state. To preserve the cargo density, we used a cargo influx rate of $\alpha/2$ at both ends. To account for reversals, we allowed cargoes to change direction with reversal rate β, but only when they were in the stopping state. To implement this in the model, we defined distinct anterograde and retrograde stopping states, S_A and S_R, and set the transition rate from the waiting state W to the stopping states to $\gamma_2 = 0.5 \times 10^3\,s^{-1}$, which is half of the value used for the unidirectional transport simulations. The transition states for this bidirectional model are shown in figure 2*c*.

A consequence of allowing stopping cargoes to reverse direction is a reduction in their tendency to form pileups. Figure 8*a* shows the trajectories of the cargoes in the initial 0.6 h of the simulations. We started with an empty axon and injected cargoes from both ends. To observe the

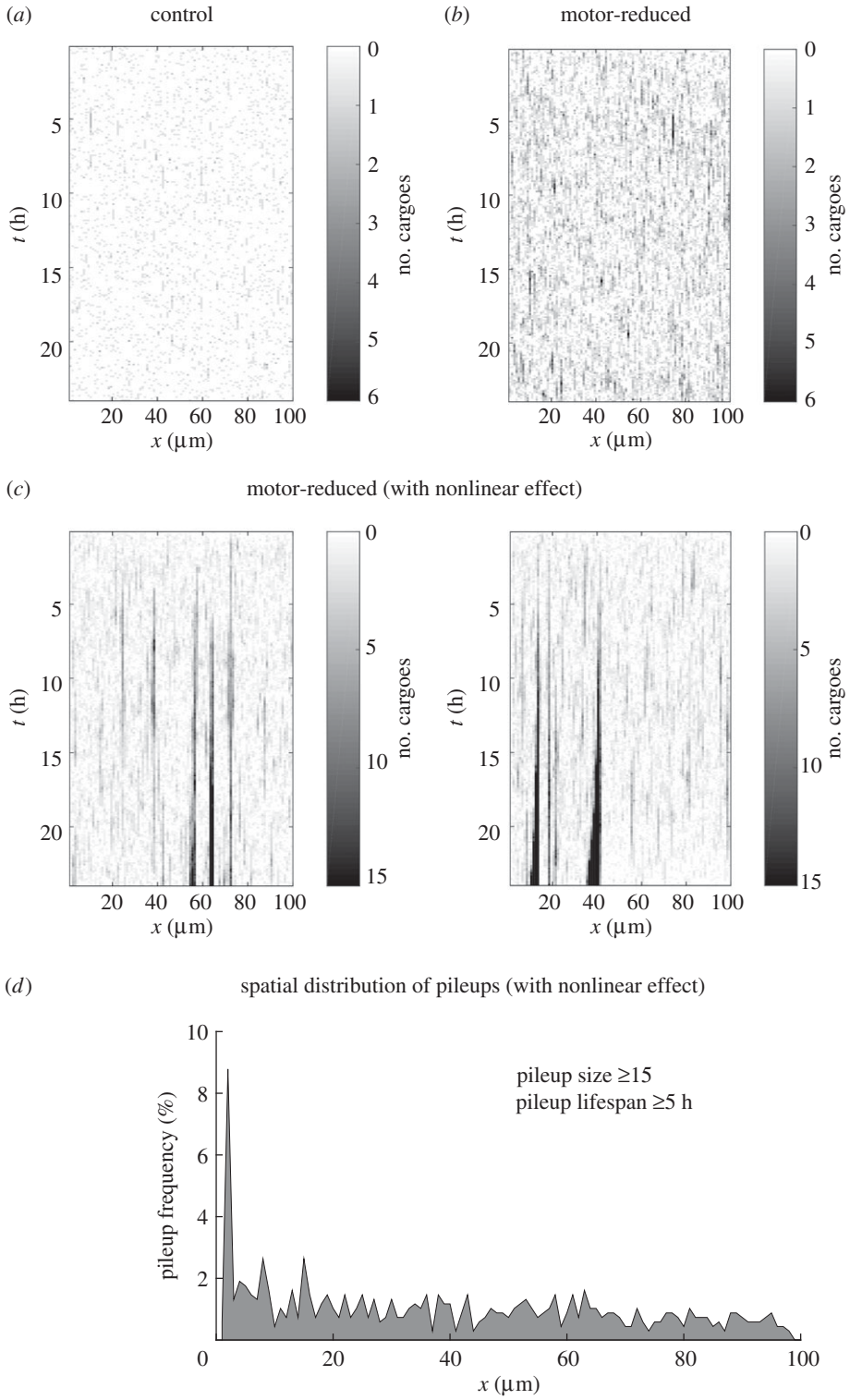

Figure 7. Spatial and temporal distribution of total cargoes with unidirectional transport in multiple lanes. (*a*) Normal axon. (*b*) Motor-reduced axon with constant moving rate ($\lambda = 1\,s^{-1}$) and constant stopping transition rate ($k_2 = 5\,s^{-1}$). (*c*) Two realizations for a motor-reduced axon with a nonlinear moving rate λ_{ij} (*i*th box, *j*th lane) with $\eta = 0.3$. (*d*) Spatial distribution of pileups with lifespans of ≥ 5 h. Since the number of lanes of traffic was increased to 5, we redefined a pileup as the accumulation of ≥ 15 cargoes at a single location along the axon (five times greater than for our simulations of one lane of traffic). Data were obtained with 1000 realizations for nonlinear λ_{ij} and $\eta = 0.3$. All other parameters were the same as in table 1.

trajectories and interactions of the cargoes more clearly, we simulated the bidirectional transport of cargoes in a single lane. We see that for large reversal rates ($\beta = 1$), the cargoes changed direction frequently so that they passed through the whole axon slowly. We also observed that many of the cargoes left the axon from the end that they entered, leading to less traffic in the axon and few cargo collisions. However, for smaller reversal rates ($\beta = 0$ in the extreme), the cargoes changed direction less frequently, moving more persistently, which resulted in more traffic and more cargo collisions.

Finally, we investigated the cargo distribution with bidirectional transport in multiple lanes on a longer time scale with a nonlinear effect of cargo crowding. To implement this, we defined the moving rate λ_{ij} of anterograde cargoes to be the same as in the unidirectional case, and the

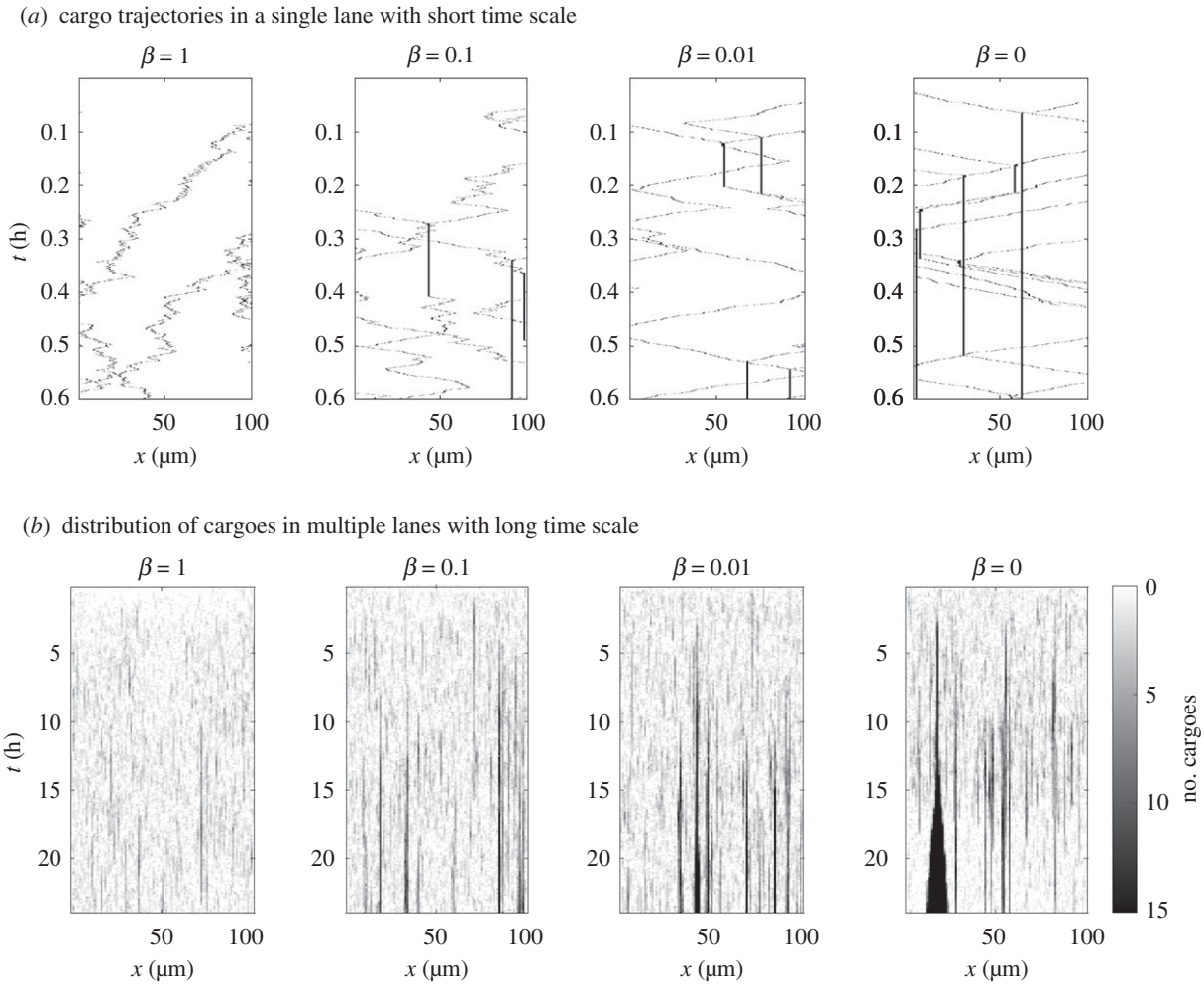

Figure 8. Spatial and temporal distribution of total cargoes with bidirectional transport. (*a*) The trajectories of cargoes in the initial 0.6 h of the simulations for motor-reduced axons with a single lane of traffic, a fixed moving rate λ_{ij}, and different reversal rates $\beta = 1, 0.1, 0.01, 0$. (*b*) The distribution of cargoes in motor-reduced axons with multiple lanes of traffic, a nonlinear moving rate (λ_{ij} with $\eta = 0.3$), and different reversal rates $\beta = 1, 0.1, 0.01, 0$. Starting with an empty axon, cargoes were allowed to enter the axon from both the proximal and distal (left and right) ends of the domain at an influx rate of $\alpha/2$. Other parameter values were the same as in table 1.

moving rate λ_{ij} of retrograde cargoes to be

$$\lambda_{ij} = \frac{\lambda}{1 + \eta \sum_{j=1}^{N_L} b_j[(a_i W_{i,j} + (1 - a_i) W_{i-1,j}]}.$$

In control axons, simulations with this nonlinear moving rate λ_{ij} yielded cargo distributions that were similar to the unidirectional case, and this was the case for all values of $\beta = 0$, 0.01, 0.1, 1 that we examined (data not shown). However, in motor-reduced axons, we observed local cargo accumulations that depended on the reversal rate β. When β was large ($\beta = 1$), pileups formed and resolved dynamically as in the case of unidirectional transport, but when β was small ($\beta = 0$, 0.01, 0.1), pileups that formed tended to grow in size, getting larger and larger over time and not dispersing, as shown in figure 8*b*. Thus, the potential for traffic pileups was very sensitive to the ability of the cargoes to reverse direction.

In addition to reversals, the formation of pileups was also sensitive to the lane-switching rate δ. Frequent lane-switching allowed a cargo that stopped due to a collision with another cargo to switch tracks and resume movement in another lane, reducing the formation of pileups. Figure 9*a* shows the temporal and spatial evolution of the axonal cargo distribution for different combinations of lane-switching rate δ and reversal rate β. When $\beta = 0.1$ and $\delta = 10$, the cargoes changed direction frequently and switched lanes frequently so that they passed through the axon slowly with relatively few collisions. In contrast with a smaller reversal rate $\beta = 0.01$ and/or smaller lane-switching rate $\delta = 0.1$, the number of pileups in the axon increased (see figure 9*c*), resulting in an increase in the total number of axonal cargoes (see figure 9*b*).

4. Discussion

In this paper, we investigated the underlying mechanism of focal cargo accumulation induced by a global reduction of functional molecular motors in axons. We hypothesized that (1) a reduction in motor number leads to a reduction in the number of active motors on each cargo, (2) this, in turn, leads to less persistent movement, more frequent stops, and thus shorter runs, (3) as cargoes stop more frequently, they impede the passage of other cargoes, leading to local 'traffic jams' and (4) collisions between moving and pausing cargoes can push pausing cargoes further away from microtubule tracks, preventing them from reattaching to microtubules and leading to the evolution of local cargo accumulations. We used a lattice-based model to test whether this mechanism can

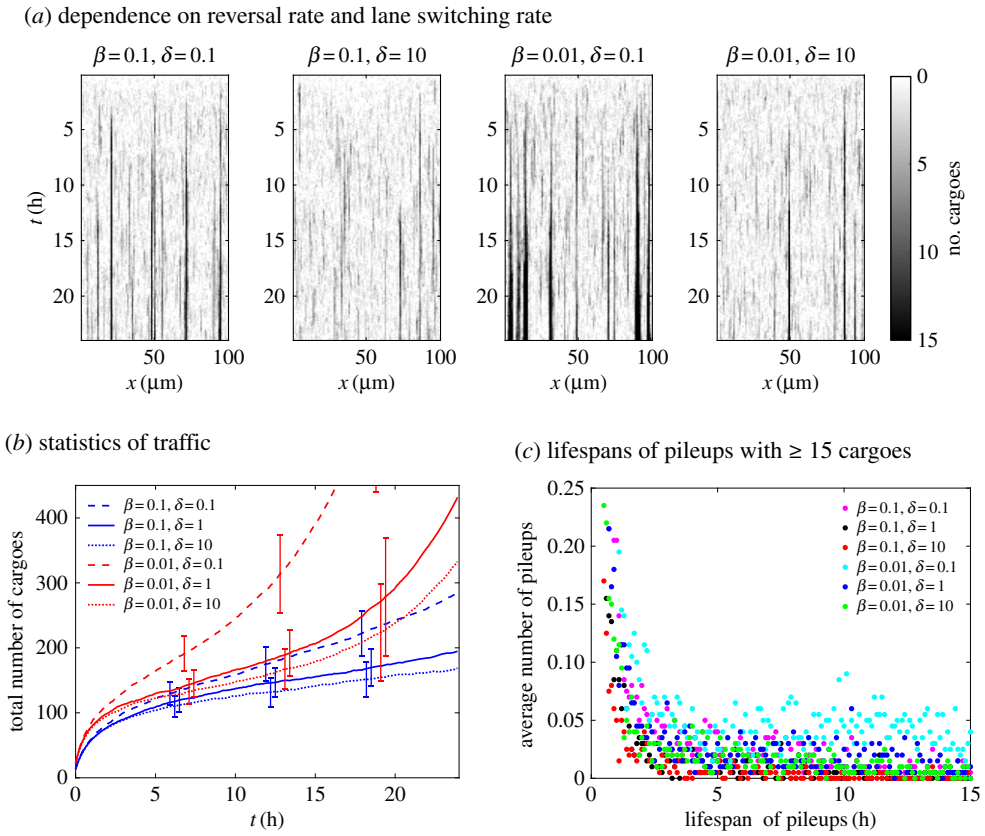

Figure 9. The effect of lane-switching on cargo pileups for the case of bidirectional traffic in multiple lanes and a nonlinear moving rate λ_{ij}. (*a*) Spatial and temporal distribution of total cargoes with bidirectional transport in motor-reduced axons for different combinations of reversal rate β and lane-switching rate δ. (*b*) Cargo accumulation in the axons versus time for different combinations of reversal rate β and lane-switching rate δ. The lines represent the total number of cargoes in the whole domain of the axon (averaged over 200 realizations; error bars represent standard deviation). (*c*) Distribution pileup lifespans (averaged over 200 realizations) for different combinations of reversal rate β and lane-switching rate δ. Here pileups with an accumulation of $\geq$15 cargoes (five times greater than for our simulations of one lane of traffic) are counted. Other parameter values were the same as in table 1.

lead to the cargo accumulation patterns observed in experiments.

We recognize that axonal cargo accumulations in disease may be caused by multiple different mechanisms, not all related to a depletion of the motor number. For example, the destabilization and fragmentation of microtubule tracks have been implicated in the aetiology of axonal transport impairments in Alzheimer's disease and some forms of hereditary spastic paraplegia [64]. In addition, cargo accumulations could also arise in axons due to aberrant local signalling that might regulate motor activity or motor interaction with its cargo or microtubule track [65]. However, while these molecular mechanisms differ, all may result in an increase in cargo stoppages and/or decrease in cargo persistency and thus potentially in an increase in cargo collisions and accumulations. Thus, while our model was inspired by experimental studies on motor depletion, it may have more general applicability to other disease mechanisms.

Our model discretized the axon into boxes in the axial and radial direction and described cargo movement as stochastic jumps in position between neighbouring boxes. Initially, we did not have any cargoes in the domain but let cargoes enter or exit the axon at the boundaries (i.e. the proximal and distal ends of the axon). We assumed that the cargo influx rate was constant, which seems reasonable on the time course of our simulations. To simulate a reduction in motor number, we altered two parameters of the model: the transition rate from moving to pausing k_2, which dictates the stopping frequency, and the persistence parameter p, which describes the likelihood that a moving cargo will continue to move when it encounters a pausing cargo. In control axons, we assumed a small k_2 and a large p, while in the motor-reduced axons we assumed a large k_2 and a small p.

Simulations of our model with unidirectional cargo transport showed that the total number of cargoes in the axonal domain increased as we increased the stopping transition rate k_2 or decreased the moving persistence rate p. This arose because the cargoes moved less persistently, pausing more often and thus had a longer residence time in the axonal domain. Increases in cargo density have also been reported in motor-depleted axons experimentally [28,29]. Under normal conditions, the number of molecular motors on the cargoes was sufficient to ensure that moving cargoes could push pausing cargoes that they collide with aside, preventing unwanted cargo accumulation and ensuring robust intracellular transport with limited traffic jams. As we increased k_2 or decreased p, we observed increasing numbers of collisions between cargoes and the formation of focal accumulations that persisted for a few hours and then resolved stochastically. This appears similar to the dynamic pileups observed in [30], though the lifetime of those pileups could not be quantified in that study due to the short time frame of the time-lapse movies.

To explore the possibility that cargo transport might be impaired in areas of cargo accumulation (e.g. due to an increased resistance to movement in areas of high cargo density), we also investigated the influence of a density-dependent stopping transition rate k_2^i, which resulted in more

frequent pauses in more crowded regions of the axon. Under these conditions, we observed the formation of persistent pileups that became larger over time. The location of the pileups had a biphasic distribution: they occurred more frequently closest to their point of entry into the axon, but at about the same frequency at locations in the interior. Persistent pileups were also observed if we assumed a nonlinear density-dependent movement rate λ. Such density-dependent effects on the moving or pausing behaviour of cargoes could explain the large focal accumulations of membranous organelles reported experimentally in motor-depleted axons [28] (figure 1).

When we extended the model further to consider the bidirectional movement of cargoes (both anterograde and retrograde) in multiple lanes, we found that the occurrence of local cargo accumulations also depended on the reversal and lane-switching rates of the pausing cargoes. For large reversal and lane-switching rates, there were few pileups because cargoes could reverse direction or switch lanes when they stopped, but for small reversal and lane-switching rates, excessive local accumulations of cargoes with long persistence times were observed under similar conditions as in the case of unidirectional transport in a single lane. In this case, we used the same entrance rate of cargoes at the two ends. However, the ratio of anterograde to retrograde transport could be different depending on their location along an axon. Since we did not find experimental data supporting this possibility, we left it as future work to explore how different entrance rates at the two ends affect the location of the pileup.

Collectively, our simulations support the hypothesis that collisions with pausing cargoes can explain the focal cargo accumulations observed in axons that experience a global reduction in functional motors such as reported in the experimental studies of [28,30], and potentially also in neurodegenerative diseases caused by mutations that impair motor protein activity (see Introduction). Two central predictions of this hypothesis are that the cargo movement in axons is impaired when moving cargoes encounter pausing cargoes, as demonstrated by the dependence of the cargo accumulation on the stopping transition rate k_2 and the moving persistence rate p, and that cargoes stop more often in areas of greater cargo density. Our simulations also imply that under normal conditions, the concentration of molecular motors in the axon must be high enough so that there are a number of active motors on the cargo surfaces, which results in persistent movement of the cargoes. This in turn ensures robust intracellular transport and avoids traffic jams. Moving forward, it will be important to test these predictions experimentally. Important questions are: what is the traffic density of cargoes along microtubules in axons, how often do cargoes collide in axons, what are the outcomes of those collisions, and what is the dependence of the kinetics of cargo transport on cargo density? For example, do cargoes pause or reverse more often at sites where other cargoes have accumulated, and what is the impact of the lane-switching ability of a motor on the susceptibility of its cargo to traffic jams in axons? Some of these questions could be answered by a systematic quantitative analysis of organelle movement in axons of control and motor-depleted neurons. While our present study is theoretical, it serves to focus our attention on the importance of such questions for understanding how cargo accumulates in axons in disease and why such accumulations do not occur in healthy axons.

Data accessibility. The dataset supporting the conclusions of this article is included within the article.

Authors' contributions. X.L., C.X. and A.B. developed and simulated the model and wrote the final manuscript. All authors read and approved the final manuscript.

Competing interests. We declare we have no competing interests.

Funding. This research is supported by NSF CAREER Award DMS 1553637 (C.X.), the Mathematical Biosciences Institute at the OSU (C.X.), the National Natural Science Foundation of China (grant no. 11501568) (X.L.), NIH grant no. R01 NS038526 (A.B.) and NSF grant no. IOS 1656784 (A.B.).

References

1. Maday S, Twelvetrees AE, Moughamian AJ, Holzbaur EL. 2014 Axonal transport: cargo-specific mechanisms of motility and regulation. *Neuron* **84**, 292–309. (doi:10.1016/j.neuron.2014.10.019)
2. Brown A. 2015 Axonal transport. In *Neuroscience in the 21st century: from basic to clinical* (eds NDV Donald, W Pfaff), pp. 333–379. New York, NY: Springer Publishing.
3. Hirokawa N, Noda Y, Tanaka Y, Niwa S. 2009 Kinesin superfamily motor proteins and intracellular transport. *Nat. Rev. Mol. Cell Biol.* **10**, 682–696. (doi:10.1038/nrm2774)
4. Hirokawa N, Niwa S, Tanaka Y. 2010 Molecular motors in neurons: transport mechanisms and roles in brain function, development, and disease. *Neuron* **68**, 610–638. (doi:10.1016/j.neuron.2010.09.039)
5. Reck-Peterson SL, Redwine WB, Vale RD, Carter AP. 2018 The cytoplasmic dynein transport machinery and its many cargoes. *Nat. Rev. Mol. Cell Biol.* **19**, 382–398. (doi:10.1038/s41580-018-0004-3)
6. Aridor M, Hannan LA. 2000 Traffic jam: a compendium of human diseases that affect intracellular transport processes. *Traffic* **1**, 836–851. (doi:10.1034/j.1600-0854.2000.011104.x)
7. De Vos KJ, Grierson AJ, Ackerley S, Miller CC. 2008 Role of axonal transport in neurodegenerative diseases. *Annu. Rev. Neurosci.* **31**, 151–173. (doi:10.1146/annurev.neuro.31.061307.090711)
8. Morfini GA *et al.* 2009 Axonal transport defects in neurodegenerative diseases. *J. Neurosci.* **29**, 12 776–12 786. (doi:10.1523/JNEUROSCI.3463-09.2009)
9. Perlson E, Maday S, Fu M-M, Moughamian AJ, Holzbaur EL. 2010 Retrograde axonal transport: pathways to cell death? *Trends Neurosci.* **33**, 335–344. (doi:10.1016/j.tins.2010.03.006)
10. Goldstein LS. 2012 Axonal transport and neurodegenerative disease: can we see the elephant? *Prog. Neurobiol.* **99**, 186–190. (doi:10.1016/j.pneurobio.2012.03.006)
11. Millecamps S, Julien J-P. 2013 Axonal transport deficits and neurodegenerative diseases. *Nat. Rev. Neurosci.* **14**, 161–176. (doi:10.1038/nrn3380)
12. Bucci C, Bakke O, Progida C. 2012 Charcot–Marie–Tooth disease and intracellular traffic. *Prog. Neurobiol.* **99**, 191–225. (doi:10.1016/j.pneurobio.2012.03.003)
13. Sasaki S, Maruyama S, Yamane K, Sakuma H, Takeishi M. 1990 Ultrastructure of swollen proximal axons of anterior horn neurons in motor neuron disease. *J. Neurol. Sci.* **97**, 233–240. (doi:10.1016/0022-510X(90)90221-8)
14. Coleman M. 2005 Axon degeneration mechanisms: commonality amid diversity. *Nat. Rev. Neurosci.* **6**, 889–898. (doi:10.1038/nrn1788)
15. Gunawardena S, Goldstein LS. 2005 Polyglutamine diseases and transport problems: deadly traffic jams on neuronal highways. *Arch. Neurol.* **62**, 46–51. (doi:10.1001/archneur.62.1.46)
16. Fabrizi GM, Cavallaro T, Angiari C, Cabrini I, Taioli F, Malerba G, Bertolasi L, Rizzuto N. 2006 Charcot–

Marie–Tooth disease type 2e, a disorder of the cytoskeleton. *Brain* **130**, 394–403. (doi:10.1093/brain/awl284)

17. Li H, Li S-H, Yu Z-X, Shelbourne P, Li X-J. 2001 Huntingtin aggregate-associated axonal degeneration is an early pathological event in Huntington's disease mice. *J. Neurosci.* **21**, 8473–8481. (doi:10.1523/JNEUROSCI.21-21-08473.2001)
18. Stokin GB *et al.* 2005 Axonopathy and transport deficits early in the pathogenesis of Alzheimer's disease. *Science* **307**, 1282–1288. (doi:10.1126/science.1105681)
19. Wirths O, Weis J, Szczygielski J, Multhaup G, Bayer TA. 2006 Axonopathy in an APP/PS1 transgenic mouse model of Alzheimer's disease. *Acta Neuropathol.* **111**, 312–319. (doi:10.1007/s00401-006-0041-4)
20. Tarrade A *et al.* 2006 A mutation of spastin is responsible for swellings and impairment of transport in a region of axon characterized by changes in microtubule composition. *Hum. Mol. Genet.* **15**, 3544–3558. (doi:10.1093/hmg/ddl431)
21. Ebbing B, Mann K, Starosta A, Jaud J, Schöls L, Schüle R, Woehlke G. 2008 Effect of spastic paraplegia mutations in kif5a kinesin on transport activity. *Hum. Mol. Genet.* **17**, 1245–1252. (doi:10.1093/hmg/ddn014)
22. Liu Y-T *et al.* 2014 Extended phenotypic spectrum of kif5a mutations: from spastic paraplegia to axonal neuropathy. *Neurology* **83**, 612–619. (doi:10.1212/WNL.0000000000000691)
23. Brenner D *et al.* 2018 Hot-spot kif5a mutations cause familial ALS. *Brain* **141**, 688–697. (doi:10.1093/brain/awx370)
24. Harms M *et al.* 2012 Mutations in the tail domain of dync1h1 cause dominant spinal muscular atrophy. *Neurology* **78**, 1714–1720. (doi:10.1212/WNL.0b013e3182556c05)
25. Hoang HT, Schlager MA, Carter AP, Bullock SL. 2017 Dync1h1 mutations associated with neurological diseases compromise processivity of dynein-dynactin-cargo adaptor complexes. *Proc. Natl Acad. Sci. USA* **114**, E1597–E606. (doi:10.1073/pnas.1620141114)
26. Weedon M *et al.* 2011 Exome sequencing identifies a dync1h1 mutation in a large pedigree with dominant axonal Charcot-Marie-Tooth disease. *Am. J. Hum. Genet.* **89**, 308–312. (doi:10.1016/j.ajhg.2011.07.002)
27. Encalada SE, Goldstein LS. 2014 Biophysical challenges to axonal transport: motor-cargo deficiencies and neurodegeneration. *Annu. Rev. Biophys.* **43**, 141–169. (doi:10.1146/annurev-biophys-051013-022746)
28. Hurd DD, Saxton WM. 1996 Kinesin mutations cause motor neuron disease phenotypes by disrupting fast axonal transport in *Drosophila*. *Genetics* **144**, 1075–1085.
29. Martin M, Iyadurai SJ, Gassman A, Gindhart JG, Hays TS, Saxton WM. 1999 Cytoplasmic dynein, the dynactin complex, and kinesin are interdependent and essential for fast axonal transport. *Mol. Biol. Cell* **10**, 3717–3728. (doi:10.1091/mbc.10.11.3717))
30. Iacobucci GJ, Rahman NA, Valtueña AA, Nayak TK, Gunawardena S. 2014 Spatial and temporal characteristics of normal and perturbed vesicle transport. *PLoS ONE* **9**, e97237. (doi:10.1371/journal.pone.0097237)
31. Sood P, Murthy K, Kumar TV, Nonet ML, Menon GI, Koushika SP. 2017 Cargo crowding at actin-rich regions along axons causes local traffic jams in neurons. *Traffic* **19**, 166–181. (doi:10.1111/tra.12544)
32. Blum JJ, Reed MC. 1985 A model for fast axonal transport. *Cell Motil.* **5**, 507–527. (doi:10.1002/cm.970050607)
33. Blum JJ, Reed MC. 1989 A model for slow axonal transport and its application to neurofilamentous neuropathies. *Cell Motil. Cytoskeleton* **12**, 53–65. (doi:10.1002/cm.970120107)
34. Blum JJ, Reed M. 1994 Models of axonal transport: application to understanding certain neuropathies. *Neurol. Dis. Ther.* **26**, 113–113.
35. Popovic L, McKinley SA, Reed MC. 2011 A stochastic compartmental model for fast axonal transport. *SIAM J. Appl. Math.* **71**, 1531–1556. (doi:10.1137/090775385)
36. Brown A, Wang L, Jung P. 2005 Stochastic simulation of neurofilament transport in axons: the 'stop-and-go' hypothesis. *Mol. Biol. Cell* **16**, 4243–4255. (doi:10.1091/mbc.e05-02-0141)
37. Craciun G, Brown A, Friedman A. 2005 A dynamical system model of neurofilament transport in axons. *J. Theor. Biol.* **237**, 316–322. (doi:10.1016/j.jtbi.2005.04.018)
38. Jung P, Brown A. 2009 Modeling the slowing of neurofilament transport along the mouse sciatic nerve. *Phys. Biol.* **6**, 046002. (doi:10.1088/1478-3975/6/4/046002)
39. Friedman A, Craciun G. 2005 A model of intracellular transport of particles in an axon. *J. Math. Biol.* **51**, 217–246. (doi:10.1007/s00285-004-0285-3)
40. McKinley SA, Athreya A, Fricks J, Kramer PR. 2012 Asymptotic analysis of microtubule-based transport by multiple identical molecular motors. *J. Theor. Biol.* **305**, 54–69. (doi:10.1016/j.jtbi.2012.03.035)
41. Bressloff PC, Newby JM. 2013 Stochastic models of intracellular transport. *Rev. Mod. Phys.* **85**, 135. (doi:10.1103/RevModPhys.85.135)
42. Chowdhury D. 2013 Stochastic mechano-chemical kinetics of molecular motors: a multidisciplinary enterprise from a physicist's perspective. *Phys. Rep.* **529**, 1–197. (doi:10.1016/j.physrep.2013.03.005)
43. Bressloff PC. 2014 *Stochastic processes in cell biology*, vol. 41. Berlin, Germany: Springer.
44. Smith RS. 1980 The short term accumulation of axonally transported organelles in the region of localized lesions of single myelinated axons. *J. Neurocytol.* **9**, 39–65. (doi:10.1007/BF01205226)
45. Tsukita S, Ishikawa H. 1980 The movement of membranous organelles in axons, electron microscopic identification of anterogradely and retrogradely transported organelles. *J. Cell Biol.* **84**, 513–530. (doi:10.1083/jcb.84.3.513)
46. Allen RD, Weiss DG, Hayden JH, Brown DT, Fujiwake H, Simpson M. 1985 Gliding movement of and bidirectional transport along single native microtubules from squid axoplasm: evidence for an active role of microtubules in cytoplasmic transport. *J. Cell Biol.* **100**, 1736–1752. (doi:10.1083/jcb.100.5.1736)
47. Schnapp BJ, Vale RD, Sheetz MP, Reese TS. 1985 Single microtubules from squid axoplasm support bidirectional movement of organelles. *Cell* **40**, 455–462. (doi:10.1016/0092-8674(85)90160-6)
48. Aghababaie Y, Menon GI, Plischke M. 1999 Universal properties of interacting Brownian motors. *Phys. Rev. E* **59**, 2578–2586. (doi:10.1103/PhysRevE.59.2578)
49. Chai Y, Klumpp S, Müller MJI, Lipowsky R. 2009 Traffic by multiple species of molecular motors. *Phys. Rev. E Stat. Nonlin. Soft Matter Phys.* **80**, 041928. (doi:10.1103/PhysRevE.80.041928)
50. Klumpp S, Lipowsky R. 2003 Traffic of molecular motors through tube-like compartments. *J. Stat. Phys.* **113**, 233–268. (doi:10.1023/A:1025778922620)
51. Müller MJI, Klumpp S, Lipowsky R. 2005 Molecular motor traffic in a half-open tube. *J. Phys. Condens. Matter* **17**, S3839–S3850. (doi:10.1088/0953-8984/17/47/014)
52. Zhang Y. 2012 Microtubule length dependence of motor traffic in cells. *Eur. Phys. J. E Soft Matter* **35**, 101. (doi:10.1140/epje/i2012-12101-3)
53. Gross SP. 2004 Hither and yon: a review of bi-directional microtubule-based transport. *Phys. Biol.* **1**, R1–R11. (doi:10.1088/1478-3967/1/2/R01)
54. Gross SP, Vershinin M, Shubeita GT. 2007 Cargo transport: two motors are sometimes better than one. *Curr. Biol.* **17**, R478–R486. (doi:10.1016/j.cub.2007.04.025)
55. Wortman JC, Shrestha UM, Barry DM, Garcia ML, Gross SP, Yu CC. 2014 Axonal transport: how high microtubule density can compensate for boundary effects in small-caliber axons. *Biophys. J.* **106**, 813–823. (doi:10.1016/j.bpj.2013.12.047)
56. Gillespie DT. 1977 Exact stochastic simulation of coupled chemical reactions. *J. Phys. Chem.* **81**, 2340–2361. (doi:10.1021/j100540a008)
57. Gillespie DT. 2007 Stochastic simulation of chemical kinetics. *Annu. Rev. Phys. Chem.* **58**, 35–55. (doi:10.1146/annurev.physchem.58.032806.104637)
58. Brady S, Lasek R, Allen R. 1982 Fast axonal transport in extruded axoplasm from squid giant axon. *Science* **218**, 1129–1131. (doi:10.1126/science.6183745)
59. Cooper PD, Smith RS. 1974 The movement of optically detectable organelles in myelinated axons of *Xenopus laevis*. *J. Physiol.* **242**, 77–97. (doi:10.1113/jphysiol.1974.sp010695)
60. Erickson RP, Jia Z, Gross SP, Clare CY. 2011 How molecular motors are arranged on a cargo is important for vesicular transport. *PLoS Comput. Biol.* **7**, e1002032. (doi:10.1371/journal.pcbi.1002032)

61. Xue C, Shtylla B, Brown A. 2015 A stochastic multiscale model that explains the segregation of axonal microtubules and neurofilaments in neurological diseases. *PLoS Comput. Biol.* **11**, e1004406. (doi:10.1371/journal.pcbi.1004406)
62. Reis GF, Yang G, Szpankowski L, Weaver C, Shah SB, Robinson JT, Hays TS, Danuser G, Goldstein LSB. 2012 Molecular motor function in axonal transport *in vivo* probed by genetic and computational analysis in *Drosophila*. *Mol. Biol. Cell* **23**, 1700–1714. (doi:10.1091/mbc.E11-11-0938)
63. Zhang K, Osakada Y, Xie W, Cui B. 2011 Automated image analysis for tracking cargo transport in axons. *Microsc. Res. Tech.* **74**, 605–613. (doi:10.1002/jemt.20934)
64. Baas PW, Rao AN, Matamoros AJ, Leo L. 2016 Stability properties of neuronal microtubules. *Cytoskeleton* **73**, 442–460. (doi:10.1002/cm.21286)
65. Brady ST, Morfini GA. 2017 Regulation of motor proteins, axonal transport deficits and adult-onset neurodegenerative diseases. *Neurobiol. Dis.* **105**, 273–282. (doi:10.1016/j.nbd.2017.04.010)